

The Structural Transformation of a Supercooled Liquid into an Amorphous Solid

Gang Sun¹, Peter Harrowell^{1*}

¹ School of Chemistry, University of Sydney, Sydney, Australia

* Corresponding author: peter.harrowell@sydney.edu.au

5
10
15
20

The persistent problem posed by the glass transition is to develop a general atomic level description of a solidification process that is not associated with any change in the symmetry of the atomic structure. The answer proposed in this paper is to measure a configuration's capacity to restrain the motion of the constituent atoms. Previous efforts based on local topologies (1) run up against the sheer diversity of disordered structures. Unlike crystals, an amorphous solid can have more than 100 local topological arrangements (2). The random first order transition theory (3-6) enlists a related overlap parameter but this characterizes a metastable state, not the mechanical restraint of a single configuration that we need. Here we show that the instantaneous normal modes (7) can be used to define a transparent measure of atomic restraint that accounts for the difference between fragile and strong liquids (8) and the collective length scale of the supercooled liquid (9-11). We show that amorphous solidification proceeds unchanged when we exclude the selection of favoured local structures and cooperative phase behaviour through ultra-rapid cooling. These results represent a significant simplification of the description of

amorphous solidification and a powerful systematic treatment of the influence of microscopic factors based on the structural description presented here.

We shall present a local measure of particle restraint in an individual configuration that is general in its definition (requiring only differentiable potentials), efficient to calculate and definable without reference to dynamics. The approach is based on the instantaneous normal modes (INM's) and their associated eigenvalues. Previous applications of INM's to liquids have used the modes to account for the collective dynamics (7). This is not our purpose here. In this paper we use the INM's as a tool to quantify the totality of structural features that contribute to restraint. As described in the Methods, the restraint of atom j will be obtained from the mean squared displacement $\langle \Delta r_j^2 \rangle_{eq} = \langle (\vec{r}_j^0 - \vec{r}_j)^2 \rangle_{eq}$ where the equilibrium average is taken based on the harmonic approximation to the Hamiltonian and $\{\vec{r}_j^0\}$ is the local minimum of the harmonic Hamiltonian.

$\langle \Delta r_j^2 \rangle_{\tau}$, the mean squared displacement for some fixed short time interval τ . As we shall demonstrate, $\langle \Delta r_j^2 \rangle_{\tau} \neq \langle \Delta r_j^2 \rangle_{eq}$

$\langle \Delta r_j^2 \rangle_{eq}$, calculated from the normal mode analysis. Yang et al (17) made use the local DW factor calculated from the dynamical matrix. Ding et al (18) introduced a

composite order parameter consisting of the product of the Voronoi volume and the local DW factor. While acknowledging the similarities of ref. (16-18) with the present work, we point out two differences that will prove significant. The first is methodological – our use of $\langle \Delta r_j^2 \rangle_{eq}$ rather than $\langle \Delta r_j^2 \rangle_\tau$ for all temperatures allows us to completely remove dynamics from the definition of the order parameter. The second difference is conceptual – we shall argue here that the significance of the restraint order parameter is not that it ‘explains’ specific material properties (while acknowledging that the correlations exist) but that it defines the underlying structural transformation between fluid and solid.

The Configurational Restraint Parameter

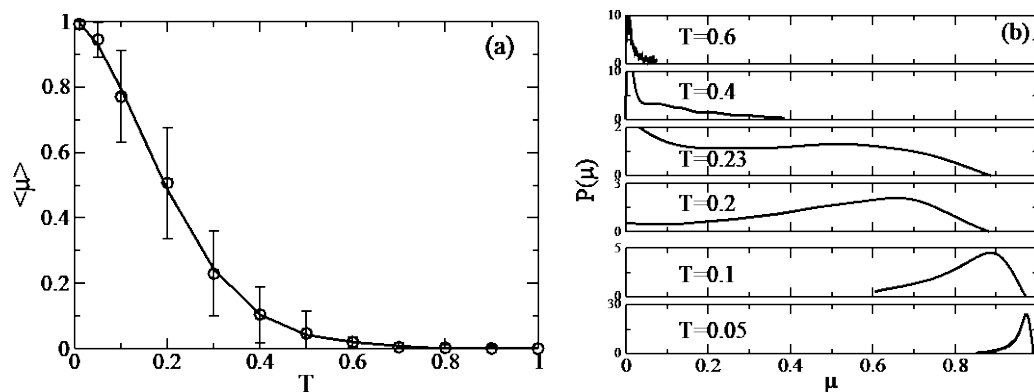
We define the *restraint* μ_j on particle j as

$$\mu_j \equiv \exp\left(-\frac{q^2 \langle \Delta r_j^2 \rangle_{eq}}{6}\right) \quad (2)$$

where q is the magnitude of the wavevector of the first peak in the structure factor $S(q)$.

In Fig. 1a we plot the average restraint $\langle \mu \rangle = \frac{1}{N} \sum_i \mu_i$ as a function of T for the binary alloy due to Kob and Andersen (KA) (19) (see Methods). The increase in μ on cooling provides an explicit measure of the progress of amorphous solidification on cooling. We find that the average restraint exhibits a nonlinear increase with decreasing T . This change is associated with the appearance of a broad binodal distribution in μ at $T \sim 0.23$ with peaks at 0 and ~ 0.5 as shown in

Fig. 1b. (For reference, the glass transition temperature based on the magnitude of the shear viscosity is $T_g \sim 0.317$ for the KA mixture (20).)



5

Figure 1. a) The plot of the average restraint $\langle \mu \rangle$ as a function of T . The vertical lines represent one standard deviation above and below the mean. b) The distribution of μ for a range of temperatures, as indicated.

10

An excellent test of the utility of the restraint parameter is to account for the striking difference between the glass transitions of oxide glass formers such as SiO_2 and the transition in liquids governed by largely isotropic interactions (i.e. molecular and metallic liquids). This difference is defined by the temperature dependence of the effective activation energy for relaxation. In the case of the network-forming liquids ('strong' in Angell's classification) the activation energy is independent of T while in molecular liquids ('fragile'), the activation energy increases with decreasing temperature (8). How do the structural transitions of these two classes of liquid differ?

15

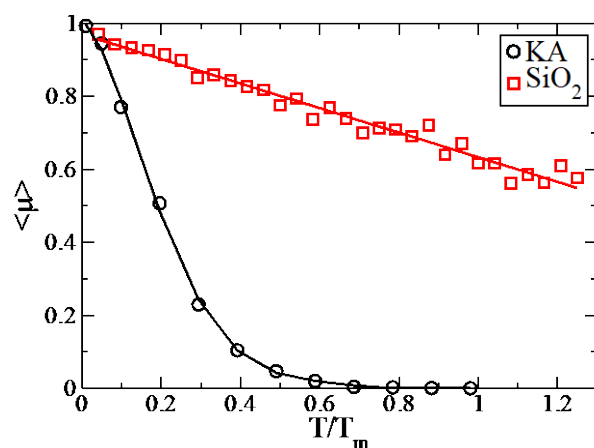


Figure 2. Plot of $\langle \mu \rangle$ vs T/T_m for the KA mixture and for silica where the melting point, T_m , is 2400K for silica (21) and 1.02 for the KA mixture (22).

5

Details of the silica simulations can be found in Methods. As shown in Fig. 2, the difference in the temperature dependence of the configurational restraint between silica and the atomic mixture is striking. Where the atomic mixture exhibits an abrupt increase in restraint at a temperature well below the melting point, silica maintains a high restraint all the way up to the boiling point. While the distinction between strong and fragile liquids has traditionally been based on their respective dynamics, we demonstrate here that these liquids can, in fact, be differentiated by structure alone. A strong liquid is one that exhibits a restraint > 0.5 at high temperatures, a value that, in Fig.1b, corresponded to the position of the first appearance of the high μ peak. From this new perspective, the puzzle posed by silica is not how it loses fluidity on cooling but, rather, how it manages to be a fluid at all.

15

Amorphous Solidification under Imposed Restraint: Pinning and Finite Size Effects

As defined above, the structural transformation from liquid to amorphous solid depends, not on the appearance of special topologies but, rather, on the presence of *any* structure capable of exerting local restraint. We can adjust this restraining influence, without any change in the configurational geometry, by pinning random particles. Let $M = (1-c)N$ be the number of unpinned particles where c is the fraction of pinned particles. Following ref. (23), the impact of pinning on the instantaneous normal modes is calculated by diagonalizing the $3M \times 3M$ Hessian matrix consisting of only derivatives of coordinates of the unpinned particles.

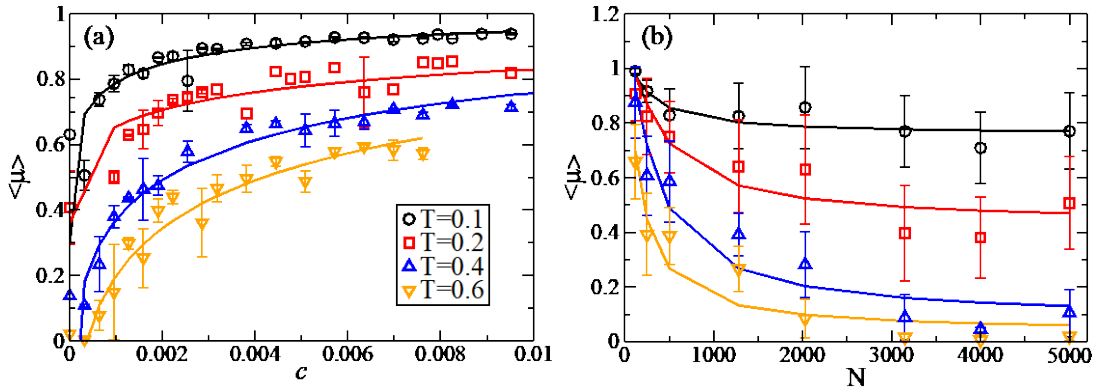


Figure 3. a) The dependence of the average restraint $\langle \mu \rangle$ as a function of the fraction of c pinned particles for a range of temperatures as indicated. The solid curves correspond to the curve in Eq.6 with fitted lengths ξ . b) Plot $\langle \mu \rangle$ vs N for a range of values of T as indicated. The solid curves are generated using Eq.7 with the length ζ fitted.

As shown in Fig. 3a, we find that the mean restraint increases quickly with the addition of a low density of pinned particles only to show signs of saturation as c is increased. This increase in $\langle \mu \rangle$ steadily shifts our fragile alloy towards the values of restraint that characterize silica in Fig.

2. This structural shift from fragility to strong due to pinning is consistent with the analogous shift in kinetic behavior reported in ref. (24). We find the following expression

$$\langle \mu(c) \rangle = 1 - (1 - \langle \mu(0) \rangle) \exp(-\xi c^{1/3}) \quad (6)$$

5

provides a satisfactory description of our data with the fitted length scale ξ increasing from 4 to 7 as T decreases from 0.6 to 0.1. The modest increase in the length ξ on cooling is similar to that reported in ref. (24). Note that here the pinning is only applied during the diagonalization of the Hessian so the associated length scale is purely mechanical in nature and not associated with thermal fluctuations.

10

A related question is the influence of system size on the amorphous solidification. In Fig. 3b we plot $\langle \mu \rangle$ vs N for different values of T. For N < 500 we find that the degree of restraint increases, indicating a fragile-to-strong transition with decreasing systems size with the N-dependence of $\langle \mu \rangle$ described by

15

$$\langle \mu(N) \rangle = 1 - (1 - \langle \mu(\infty) \rangle) \exp(-\zeta^3 / N) \quad (7)$$

The associated length ζ , obtained by fitting, is similar in magnitude and T dependence to that obtained from pinning (i.e. an increase from 5.2 to 6.55 as T decreases from 0.6 to 0.1). Gutiérrez et al (9) reported a system size dependence of the structural relaxation time of the KA mixture with a similar scaling to that observed in Fig. 3b. In ref. (9), this scaling length was found to match a length obtained directly from a normal mode analysis. The idea (10,11) is that

20

minimum eigenvalue of the inherent structure exhibits a crossover from a plastic mode to a Debye vibration as N increases, with the crossover size providing the length. The connection between this length and the one we extract here from the INM's is an interesting question. As shown in the Supplementary Material, a finite system size or non-zero pinning concentration act to decrease the density of low eigenvalue modes.

It has been proposed (25) that the transition to the amorphous solid arises as a result of the growing correlation length. The growing length indicated in Fig. 3 suggests a different interpretation, one in which the length scales arise as a *consequence* of the increasing restraint, not as the cause, and that these lengths reflect the mechanical character of the individual configurations, specifically the characteristic length scales associated with the unstable modes of the INM's, and not the result of some correlation between thermally sampled configurations.

Configurational Restraint and the Self Intermediate Scattering Function

In supercooled liquids, the self intermediate scattering function $F_s(q,t)$,

$$F_s(q,t) = \frac{1}{N} \left\langle \sum_j^N \exp(i\vec{q} \cdot \Delta\vec{r}_j(t)) \right\rangle \quad (9)$$

taken at a value of the wavevector q corresponding to the first peak of the structure factor $S(q)$, is referred to as the structural relaxation function. The decay of this function in the supercooled liquid, as shown in Fig. 4a, proceeds via a two step process; a fast relaxation to a plateau value, h , which is subsequently relaxed by slower mechanism, the α process, with a strong temperature dependence. If we assume the displacement statistics are Gaussian then

$$h \approx \exp\left(-\frac{q^2 \langle \Delta r^2 \rangle_\tau}{6}\right). \quad (10)$$

where $\langle \Delta r^2 \rangle_\tau$ is the average DW factor. Given the similarity between this approximate relaxation function and our order parameter $\langle \mu \rangle$ defined in Eq. 6, we can ask whether $\langle \mu \rangle$ is equivalent to the plateau value h of $F_s(q, t)$.

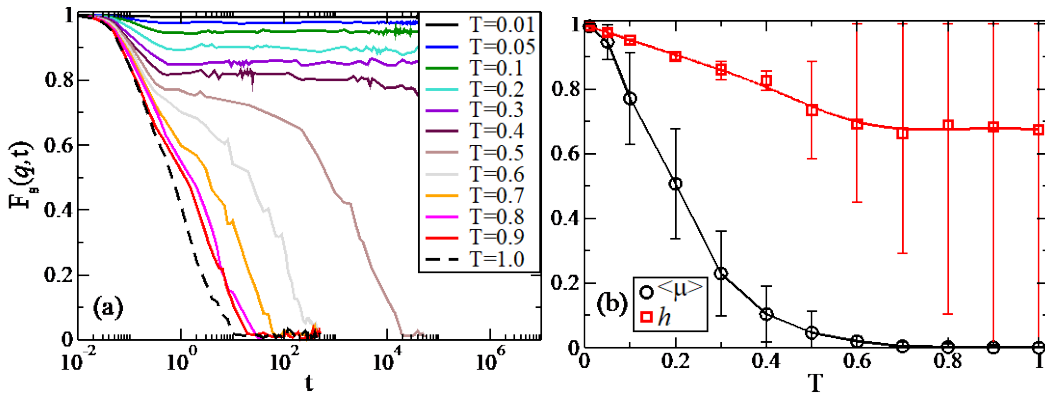


Figure 4. a) Plots of the self intermediate scattering function $F_s(q, t)$ vs log time for range of temperatures. b) Plot of the plateau height h of $F_s(q, t)$ and μ as a function of T . Note the large uncertainty in the plateau height at high T . Details of the calculation of h and the associated uncertainty are provided in the Supplementary Materials.

In Fig. 4b we establish that $\langle \mu \rangle \neq h$, with the restraint $\langle \mu \rangle$ exhibiting a much stronger dependence on temperature than h , dropping to zero over a temperature range for which the plateau exhibits only a weak variation. We also note that h becomes ill-defined for $T > 0.6$ due to the disappearance of the plateau. The fact that $\langle \mu \rangle$ is smaller than h is perhaps surprising since the former corresponds to an average over a highly restricted set of fluctuations while the latter

has no imposed constraints. The explanation is that the large amplitude fluctuations responsible for the small values of μ are not accessible to the dynamics on the lifetime of given instantaneous configuration. This observation, that the truncated lifetime of the INM's contributes to the caging of particles by preventing their access to soft modes actually present in the configuration, is an interesting new perspective that we leave to future work.

Amorphous Solidification in the Limit of High Cooling Rates

How important are cooperative processes and favored structures in amorphous solidification?

We can address this question by asking how the solidification is affected by the cooling rate.

Experimentally, cooling rates of up to 10^{14} K s⁻¹ have been achieved (26). The maximum possible quench rate ($> 10^{15}$ K s⁻¹) is achieved in simulations by carrying out a steepest decent or conjugate gradient minimization of the potential energy. As there is no meaningful temperature during rapid minimization, we shall use the potential energy per particle E_p of the instantaneous configuration as a control parameter. In the case of the conjugate gradient quench, we collect intermediate configurations during the energy minimization, calculate $\langle\mu\rangle$ and plot it against the potential energy of that configuration. For the temperature used to calculate the averages in Eqs. 2 and 3, we shall use an effective temperature obtained by mapping the potential energy E_p to the $\langle E_p \rangle$ vs T curve from the equilibrium simulations. The comparison of the dependence of the solidification on E_p for the equilibrated cooling and conjugate gradient minimization is plotted in Fig. 5.

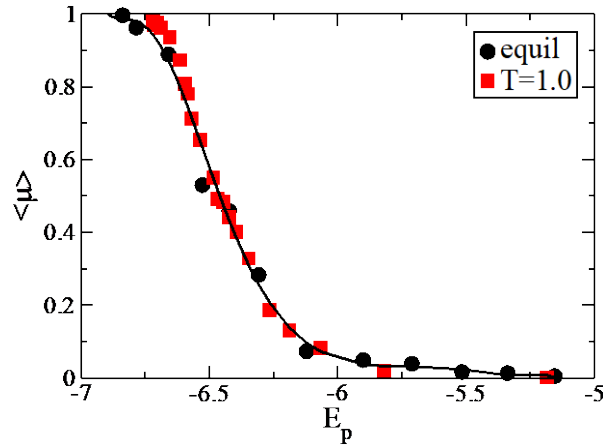


Figure 5. Restraint order parameter as function of potential energy. Black circles indicated the slow equilibrated cooling via swap MC. Red squares indicate the fast quench via minimization from initial state at $T=1.0$ ($=0.98 T_m$). The curve is included as a guide the eye.

5

The similarity between the two transformations in Fig. 5 is striking. While there is a small difference at low energies with the minimization exhibiting a slightly higher restraint than the equilibrated cooling when quenched from a high temperature liquid, the two curves are essentially equivalent overall. We conclude that, in spite of the variations in material properties on the cooling rate (27,28), the increase in $\langle \mu \rangle$ that takes place during energy minimization effectively captures the same process of amorphous solidification as observed via slow equilibrated cooling. If energy minimization from a high temperature liquid can reproduce the essential features of amorphous solidification observed at very slow cooling rates it follows that structures and correlations observed in the equilibrated low temperature liquid that are excluded in the configurations generated by energy minimization cannot be cited as causes of the solidification. We shall return to this point in the next Section.

15

Conclusion

In this paper we have demonstrated that there exists a quantifiable change in structure that provides a useful characterization of the transformation, on cooling, of a liquid into an amorphous solid. By ‘useful’ we mean we can account, in purely structural terms, for the differences in vitrification of fragile and strong liquids, the impact of imposed constraints such as pinning and finite size and provide a consistent description of amorphous solidification up to the maximum possible cooling rate. Previously (29) we have established that a related measure of restraint can account for the enhanced kinetics at a glass surface.

What of dynamics? The conventional representation of amorphous solidification is based on equating solidity with a shear viscosity in excess of some threshold value, a phenomenological view that regards slow dynamics as the primary *cause* of amorphous solidification. We have argued here that solidity can be usefully treated as a structural property, implying that dynamics arises as a *consequence* of the structural transition on cooling. While there is no shortage of empirical correlations supporting this link (12-18), establishing the theoretical connection between structure and dynamics remains a hard problem, in large part because dynamics requires more information (e.g. extent of reorganization events, reversibility, etc.) than a single configuration provides.

When the restraint is plotted against potential energy in Fig. 5, we find no significant difference between the liquids equilibrated at successively lower temperatures and a high temperature liquid subjected to conjugate gradient minimization. This equivalence is an important result. The minimization excludes, by construction, behavior such as the accumulation of favored local structures, the formation of extended polyhedral clusters or the influence of pre-transition fluctuations associated with a proposed low temperature phase transition. While these well

studied examples of cooperative behavior may be present in the equilibrated low temperature liquids, our results demonstrate that they cannot be ascribed as a cause of the amorphous solidification. Solidity, we conclude, arises as the direct mechanical consequence of the increase in Hessian matrix elements as the potential energy decreases. This mechanical picture of the glass formation extends to the associated length scale. We have shown that the length scales associated with solidification can be obtained as the consequence of purely mechanical perturbations (pinning, finite size) of individual configurations.

Amorphous solidification represents a rich field of phenomena, one littered with important practical applications and unresolved fundamental questions. The nature of amorphous surfaces, the impact of atomic association ('micro alloying'), the role of molecular shape and internal flexibility, the consequences of applied strain – all of these questions can be addressed as structural problems based on the distribution of atomic restraint through straightforward applications of the methodology introduced in this paper.

Methods

Simulation Models and Algorithms

Unless otherwise indicated, all calculations have been carried out using the $A_{80}B_{20}$ Lennard-Jones mixture introduced by Kob and Andersen (KA) (15) with 5000 particles in a simulation cell with periodic boundary conditions. As we do not require dynamic sampling relaxed configurations are generated using particle swap MC simulations (30) at constant NVT with a fixed number density of 1.2. Details of the dispersion of the INM's and the temperature dependence of the number of unstable modes are provided in the Supplementary Material.

Molten silica has been modelled with the SHIK-1 potential (31). Details of the simulations and calculation of the Hessian are provided in the Supplementary Materials. The treatment of these modes and the subsequent calculation of the restraint $\{\mu_i\}$ was carried out as for the Lennard-Jones system.

5

Calculation of the Restraint Order Parameter

We calculate $\langle \Delta r_j^2 \rangle_{eq}$ in terms of the variance of the amplitudes A_α of the instantaneous normal modes as

$$\langle \Delta r_j^2 \rangle_{eq} = \sum_{\alpha} \langle A_{\alpha}^2 \rangle_{eq} (\vec{v}_{\alpha}^j)^2 \quad (2)$$

10

where \vec{v}_{α}^j is the components of the α eigenmode arising from particle j . If the eigenvalue $\lambda_{\alpha} > 0$, the average $\langle A_{\alpha}^2 \rangle_{eq}$ can be evaluated analytically as

$$\langle A_{\alpha}^2 \rangle_{eq} = k_B T / \lambda_{\alpha} \quad (3)$$

For those unstable modes with $\lambda_{\alpha} \leq 0$, Eq. 3 cannot be used. Instead, we numerically integrate

$$\langle A_{\alpha}^2 \rangle_{eq} = \frac{\int A_{\alpha}^2 e^{-\beta U(A_{\alpha})} dA_{\alpha}}{\int e^{-\beta U(A_{\alpha})} dA_{\alpha}} \quad (4)$$

15

where $U(A_{\alpha})$ is the true potential energy calculated as a function of the variation of the amplitude A_{α} , holding all other mode amplitudes at zero and $\beta = (k_B T)^{-1}$. Details of these calculations are provided in the Supplementary Materials.

Acknowledgements

20

The authors gratefully acknowledge the assistance of Linwei Li in the generation of data for the silica system.

Funding. The authors acknowledge support from the Australian Research Council Discovery Project grant DP180104038 (PH).

Author contributions. Conceptualization - PH; Methodology - GS, PH; Calculations - GS; Writing - GS, PH

5 **Completing interests.** Authors declare they have no competing interests.

Data availability. All the data are available from the corresponding author upon reasonable request.

10 **Code availability.** The custom code and mathematical algorithms that are involved in the analysis and findings of this study are available from the corresponding author upon reasonable request.

Supplementary Materials

Additional Information on Methods

15 Figs. S1 to S7 and Reference (32)

References

1. C. P. Royal and S. R. Williams, The role of local structure in dynamical arrest, *Phys. Rep.* **560**, 1-75 (2015).
- 20 2. D. Wei, J. Yang, M.-Q. Jiang, L.-H. Dai, Y.-J. Wang, Dyre, I. Douglass and P. Harrowell, Assessing the utility of structure in amorphous materials. *J. Chem. Phys.* **150**, 114502 (2019).
3. V. Lubchenko and P. G. Wolynes, Theory of structural glasses and supercooled liquids. *Ann. Rev. Phys. Chem.* **58**, 235-266 (2007).
4. G. Parisi and F. Zamponi, Mean-field theory of hard sphere glasses and jamming. *Rev. Mod.*
25 *Phys.* **82**, 789-845 (2010).

5. S. Franz and G. Parisi, Recipes for metastable states in spin glasses. *J. Phys. I* **5**, 1401-1415 (1995)
6. B. Guiselin, G. Tarjus and L. Berthier, On the overlap between configurations in glassy liquids. *J. Chem. Phys.* **153**, 224502 (2020).
- 5 7. R. M. Stratton, The instantaneous normal modes of liquids. *Acc. Chem. Res.* **28**, 201-207 (1995).
8. C. A. Angell, Formation of glasses from liquids and biopolymers. *Science* **267**, 1924-1935 (1995).
9. R. Gutiérrez, S. Karmakar, Y. G. Pollack and I. Procaccia, The static lengthscale characterizing the glass transition at lower temperatures. *EPL* **111**, 56009 (2015).
- 10 10. S. Karmakar, E. Lerner and I. Procaccia, Direct estimate of the static length-scale accompanying the glass transition. *Physica A* **391**, 1001-1008 (2012).
11. G. Biroli, A. Karmakar and I. Procaccia, Comparison of static length scales characterizing the glass transition. *Phys. Rev. Lett.* **111**, 165701 (2013).
12. J. C. Dyre, T. Christensen and N. B. Olsen, Elastic models for the non-Arrhenius viscosity of glass-forming liquids. *J. Non-Cryst. Sol.* **352**, 4635-4642 (2006).
- 15 13. L. Larini, A. Ottochian, C. De Michele and D. Leporini, Universal scaling between structural relaxation and vibrational dynamics in glass-forming liquid and polymers. *Nature Phys.* **4**, 42-45 (2008).
14. D. S. Simmons, M. T. Cicerone, Q. Zhong, M. Tyagi and J. F. Douglas, Generalized localization model of relaxation in glass-forming liquids. *Soft Matter* **8**, 11455(2012).
- 20 15. U. Buchenau, R. Zorn and M A. Ramos, Probing cooperative liquid dynamics with the mean squared displacement. *Phys. Rev. E* **90**, 042312 (2014).
16. H. Tong and N. Xu, Order parameter for structural heterogeneity in disordered solids. *Phys. Rev. E* **90**, 010401(R) (2014).

17. X. Yang, H. Tong, W.-H. Wang and K. Chen, Emergence and percolation of rigid domains during the colloid glass transition. *Phys. Rev. E* **99**, 062610 (2019).
18. J. Ding, Y.-Q. Cheng, H. Sheng, M. Asta, R. O. Ritchie and E. Ma, Universal structural parameter to quantitatively predict metallic glass properties. *Nature Com.* **7**, 13733 (2016).
- 5 19. W. Kob and H. C. Andersen, Testing mode-coupling theory for a supercooled binary Lennard-Jones mixture – The van Hove correlation function. *Phys. Rev.* **51**, 4626-4641 (1995).
20. Y. Zhang, L. Huang and Y. Shi, Molecular dynamics study on the viscosity of glass-forming systems near and below the glass transition temperature. *J. Am. Ceram. Soc.*, doi.org/10.1111/jace.18006 (2021).
- 10 21. A. Takada, P. Richet, C. R. A. Catlow and G. D. Price, Molecular dynamics simulations of vitreous silica structures. *J. Non-Cryst. Solids* **345-346**, 224-229 (2004).
22. U. R. Pedersen, T. B. Schroder and J. C. Dyre, Phase diagram of Kob-Andersen-type binary Lennard-Jones mixtures. *Phys. Rev. Lett.* **120**, 165501 (2018).
23. L. Angelani, M. Paoluzzi, G. Parisi and G. Ruocco, Probing the non-Debye low-frequency
15 excitations in glass through random pinning. *Proc. Nat. Acad. Sci.* **115**, 8700-8704 (2018).
24. S. Chakrabarty, S. Karmakar and C. Dasgupta, Dynamics of glass forming liquids with randomly pinned particles. *Sci. Rep.* **5**, 12577 (2015).
25. S. Karmakar, C. Dasgupta and S. Sastry, Growing length scales and their relation to timescales in glass-forming liquids. *Ann. Rev. Cond. Matter Phys.* **5**, 255-284 (2014).
- 20 26. L. Zhong, J. Wang, H. Sheng, Z. Zhang and S. X. Mao, Formation of monatomic metallic glasses through ultrafast liquid quenching, *Nature* **512**, 177- 182 (2014).
27. J. Ashwin, E. Bouchbinder and I. Procaccia, Cooling-rate dependence of the shear modulus of amorphous solids. *Phys. Rev. E* **87**, 042310 (2013).

28. H. Staley, E. Flenner and G. Szamel, Cooling-rate dependence of kinetic and mechanical stabilities of simulated glasses. *J. Chem. Phys.* **142**, 244508 (2015).
29. G. Sun, S. Saw, I. Douglass and P. Harrowell, Structural origin of enhanced dynamics at the surface of a glassy alloy. *Phys. Rev. Lett.* **119**, 245501 (2017).
- 5 30. T. S. Grigera and G. Parisi, Fast Monte Carlo algorithm for supercooled soft spheres. *Phys. Rev. E* **63**, 045102 (2001).
31. S. Sundararaman, L. Huang, S. Ispas, W. Kob, New optimization scheme to obtain interaction potentials for oxide glasses. *J. Chem. Phys.* **148**, 194504 (2018).
32. V. I. Clapa, T. Kottos and F. W. Starr, Localization transition of instantaneous normal modes
10 and liquid diffusion. *J. Chem. Phys.* **136**, 144504 (2012).

5

Supplementary Materials for

The Structural Transformation of a Supercooled Liquid into an Amorphous Solid

Gang Sun, Peter Harrowell*

* Correspondence to: peter.harrowell@sydney.edu.au

10

This PDF file includes:

15

Materials and Methods
Figs. S1 to S7
Ref. 32

20

Materials and Methods

1. Simulations and Normal Mode Analysis of the KA Mixture.

5 The Monte Carlo simulations of the $A_{80}B_{20}$ Lennard-Jones mixture use the potential introduced by Kob and Andersen (15) with 5000 particles in a simulation cell with periodic boundary conditions. Well relaxed configurations are generated using particle swap Monte Carlo (MC) simulations at constant NVT with a fixed number density of 1.2.

10 To simulate the systems, we have used a Monte Carlo algorithm from the DLMONTE 2.0 version suite of software. The random walk in the MC simulations is constructed using a Metropolis scheme that iterates the following three steps:

1. Select a particle i at random and calculate its energy $U(\mathbf{r}_1)$.
2. Draw 8 random numbers r_1, \dots, r_8 uniform in $0,1$. Generate a standard MC trial move [i.e., shift particle by $\Delta \mathbf{r} = (2r_2-1, 2r_3-1, 2r_4-1)\Delta r$], $\mathbf{r}_2 = \mathbf{r}_1 + \Delta \mathbf{r}$. Calculate its new energy $U(\mathbf{r}_2)$.
3. Accept or reject the particle displacement according to the Metropolis acceptance rule:
 $P_{acc}(\mathbf{r}_1 \rightarrow \mathbf{r}_2) = \min(1, \exp\{-\beta[U(\mathbf{r}_2) - U(\mathbf{r}_1)]\})$

Swap moves are also applied in this work, with the exchange frequency $n=50$ time steps. The details are as follows:

4. Choose a random particle j of a different type.
5. Swap particle positions $\mathbf{r}_j \leftrightarrow \mathbf{r}_i$. Shift both particles as in the standard move
 $[\Delta \mathbf{r}_i = (2r_2-1, 2r_3-1, 2r_4-1)\Delta r, \Delta \mathbf{r}_j = (2r_5-1, 2r_6-1, 2r_7-1)\Delta r]$.
6. Accept or reject new configuration according to the Metropolis criterion
7. Repeat for all particles.

25 The calculation of the variance of the amplitude A_k of mode k for cases where the eigenvalue $\lambda_k < 0$ were carried out as follows.

30 A 1D energy curve can be plotted based on the variation of the potential energy U with respect to the selected amplitude A_k while setting all other mode amplitudes to zero. The results for two such curves are shown in Fig. S1, one with $\lambda_k < 0$ and one with $\lambda_k > 0$. In the case of the $\lambda_k < 0$ mode we see the region of negative curvature. While the value of $\langle A_k^2 \rangle$ can be calculated analytically for the $\lambda_k > 0$ case, as indicated by Eq. 3 in the paper, $\langle A_k^2 \rangle$ must be calculated numerically when $\lambda_k < 0$. As can be seen from Fig. S1, this variance is well defined due to the positive contributions of higher order terms in A_k . The numerical integration indicated in Eq. 4 is carried out over the range of A_k for which $\Delta E \leq 10k_B T$ as indicated in Fig. S1. Increasing this threshold produces no change in the calculated value. is chosen as energy threshold.

35 In Fig. S2 we plot the temperature dependence of the fraction of modes with negative eigenvalues and the distributions of average square $\langle A_\alpha^2 \rangle$'s from the stable and unstable modes. We find that the fraction of unstable modes decreases monotonically with decreasing T and vanishes at $T \sim 0$. As similar variation of f with T has been reported previously (31). As shown in Fig. S2b, the amplitudes associated with the unstable modes, evaluated using Eq. 4, are very much larger than those of the stable modes and so contribute significantly to the magnitude of $\langle \Delta r_j^2 \rangle$.

2. Simulations of the SHK Silica and Calculation of the Hessian

45 We perform the molecular dynamics (MD) simulations of silica by using SHIK-1 potentials (19) which have high geometric accuracy. This potential includes long range Coulomb interactions requiring an Ewald sum. The silica systems contain 576 atoms. All the samples are prepared using the melt-quench method. At first, we generate an Alpha-quartz model at 300 K, then we relaxed the quartz at 300K, zero pressure condition for 0.1 ns to release the

pressure. After the quartz was relaxed, we heated the quartz to 4000 K at a constant rate over 0.5 ns, then equilibrated the melted sample at a density of 2.2 g/cm³ for another 0.5 ns in the NVT ensemble. The sample was then quenched to 300 K in the NPT ensemble at a rate of 1 K/ps with zero pressure. After quenching, it was then annealed at 300 K for another 1 ns.

5

Hessian matrix elements are usually defined as,

$$H_{\mu,\nu} = \frac{1}{\sqrt{m_i m_j}} \frac{\partial^2 U}{\partial r_{i,\alpha} \partial r_{j,\beta}} (i, j = 1, \dots, N, \mu, \nu = x, y, z) \quad (\text{S1})$$

10

Where U is the total potential energy of the system. Since long range interactions are involved in the simulation of silica, analytical expressions for the Hessian matrix elements are complicated. Therefore, we generated the Hessian matrix moving the individual particles from their starting configuration R to $R + \delta r_{j,\nu}$, in order to counterbalance, a double move of R to $R - \delta r_{j,\nu}$, is employed. The displacement of 0.0016 Å has been chosen as it is small enough to avoid any disruption to the structure and gives reasonably accurate result.

15

$$\sqrt{m_i m_j} H_{\mu,\nu} = \nabla_{i,\mu} \nabla_{j,\nu} U = \frac{f_{i,\mu}(R + \delta r_{j,\nu}) - f_{i,\mu}(R - \delta r_{j,\nu})}{2\delta r_{j,\nu}} \quad (\text{S2})$$

The details of how to obtain the small displacement in our simulation are shown as follows. The three axis vectors \vec{A} , \vec{B} and \vec{C} , expressed in x, y and z Cartesian Coordinates as follows,

20

$$\vec{A} = (x_{hi} - x_{lo}, 0, 0) = (\Delta x, 0, 0)$$

$$\vec{B} = (x_{y}, y_{hi} - y_{lo}, 0) = (x_{y}, \Delta y, 0)$$

$$\vec{C} = (x_{z}, y_{z}, z_{hi} - z_{lo}) = (0, 0, \Delta z)$$

$$\vec{r}_j = (x_j, y_j, z_j) = n_A \vec{A} + n_B \vec{B} + n_C \vec{C}$$

$$\left\{ \begin{array}{l} n_A = \frac{x_j - \frac{y_j}{\Delta y} (x_{y})}{\Delta x} \\ n_B = y_j / \Delta y \\ n_C = z_j / \Delta z \end{array} \right. \quad \text{and} \quad \left\{ \begin{array}{l} L_x = |A| \\ L_y = |B| \\ L_z = |C| \end{array} \right.$$

25

$$\Delta \vec{r} = \vec{r}_j - \vec{r}_i = (n_A^j - n_A^i) \vec{A} + (n_B^j - n_B^i) \vec{B} + (n_C^j - n_C^i) \vec{C}$$

$$\Delta n_A = (n_A^j - n_A^i)$$

$$\left\{ \begin{array}{l} \text{if } (\Delta n_A > 0.5) \Delta n_A = \Delta n_A - 1 \\ \text{if } (\Delta n_A < -0.5) \Delta n_A = \Delta n_A + 1 \end{array} \right.$$

The same procedure is applied to the other two directions, \vec{B} and \vec{C} .

30

On diagonalizing the Hessian we find a fraction f of modes with negative eigenvalues that decreases monotonically with temperature and appears to vanish at T = 0 as shown in Fig. S3.

3. Effect of Pinning and System Size on the Distribution of Normal Modes

The impact of pinning concentration and system size on the restraint order parameter arise from the impact of these parameters on the density of states in the harmonic analysis. This can be seen in Fig. S4 which shows an increase in small amplitude modes and a decrease in small eigenvalue λ modes when we either increase c , the pinning concentration, or decrease N , the system size.

4. Calculation of Plateau Height h and its Associated Error

For supercooled liquids, the self intermediate scattering function $F_s(q,t)$, is taken at the a value of the wavevector $q=q_1$, which corresponds to the first peak of the structure factor $S(q)$. The structure factor as function of wavevector is shown in Fig.S2.

For liquids, the relaxation occurs in two steps, observed from the self intermediate scattering function $F_s(q_1,t)$ [see Fig.S6]. The two step decays correspond to α relaxation (slow) and β relaxation (fast). Hence, it is reasonable to fit $F_s(q,t)$ of liquids by a sum of two functions,

$$F_s(q_1,t) = (1-h) \exp \left[-\left(\frac{t}{\tau_\beta} \right)^2 \right] + h \exp \left[-\left(\frac{t}{\tau_\alpha} \right) \right] \quad (S3)$$

where h is the plateau height of relaxation function F_s . The quality of the fits is demonstrated in two examples plotted in Fig. S6.

The quality of the fit is measured by the correlation coefficient ε between the fitted curves and the intermediate scattering function $F_s(q_1,t)$. What we would like to establish is how ε varies with the value of h . To estimate the uncertainty in the value of we have proceeded as follows.

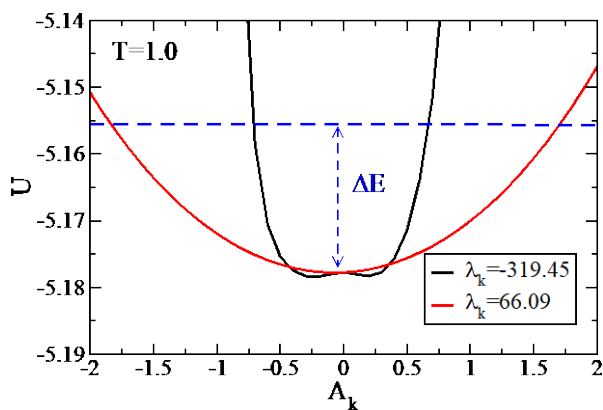
Step 1. Fit the intermediate scattering function $F_s(q_1,t)$ with the Eq.(S3), and let $h=h^*$.

Step 2. Fix $h=h^*+\delta$ and redo the fit over the 2 remaining variables and record the overall measure of the quality ε of the new fit.

Step3. Repeat this for a range of δ 's, +ve and -ve, and plot ε as a function of δ . The result is plotted in Fig. S7. As expected, there is an extremum at $\delta = 0$, i.e. the original fit returned the best value of h . What we are interested in is the curvature about the extremum. If it is high curvature then it means that the uncertainty in the original value of h was small. If the curvature is low, i.e. varying h does not change the quality of fit, then the uncertainty in h is high. The uncertainty in h can be estimated by the interval in δ over which ε lies above some threshold value, here $\varepsilon > 0.95$.

References

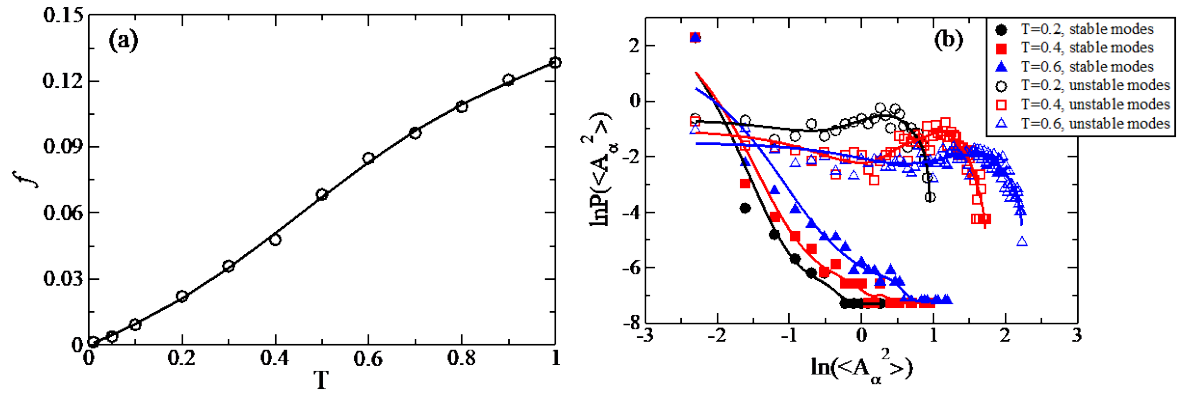
19. W. Kob and H. C. Andersen, Testing mode-coupling theory for a supercooled binary Lennard-Jones mixture – The van Hove correlation function. *Phys. Rev.* **51**, 4626-4641 (1995).
31. S. Sundararaman, L. Huang, S. Ispas, W. Kob, New optimization scheme to obtain interaction potentials for oxide glasses. *J. Chem. Phys.* **148**, 194504 (2018).
32. V. I. Clapa, T. Kottos and F. W. Starr, Localization transition of instantaneous normal modes and liquid diffusion. *J. Chem. Phys.* **136**, 144504 (2012).



5

Figure S1. The potential energy as function of fluctuation amplitude A_k of mode k at a configuration from $T=1.0$ for two modes with eigenvalues λ_k as indicated.

5



10

Figure S2. a) The fraction of unstable modes as a function of T . b) The log-log plot of the distribution of mode amplitudes $\langle A_\alpha^2 \rangle$'s from the stable and unstable modes at $T = 0.6$ and 0.2 . The curves are fits included as a visual guide.

5

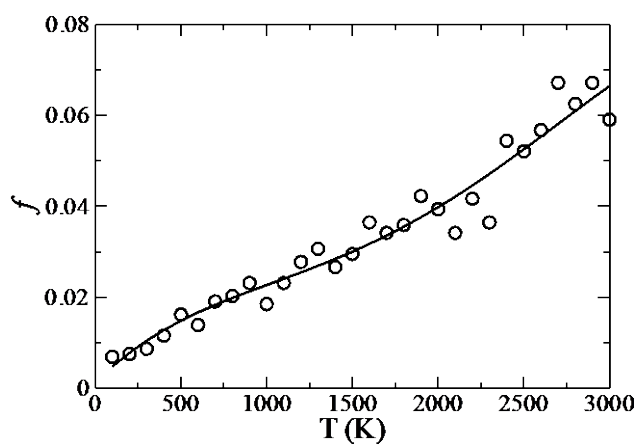


Figure S3. The fraction of unstable modes of silica as function of T .

5

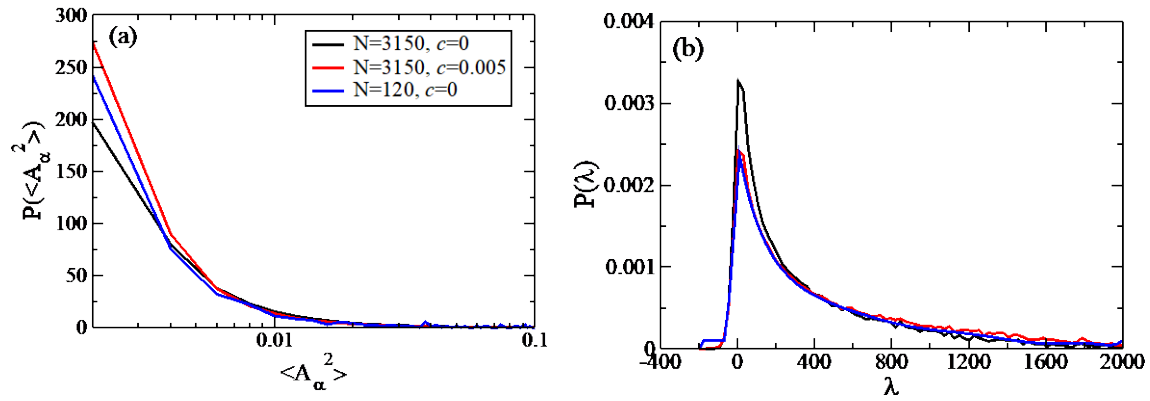


Figure S4. (a) The distribution of the square amplitudes for each mode at $T=0.6$. (b) The distribution of eigenvalues of Hessian Matrix for instantaneous structure from $T=0.6$. Here we include three different systems with system particle number $N=120$ and 3150 , and pinning particle concentration $c=0$ and 0.05 .

10

5

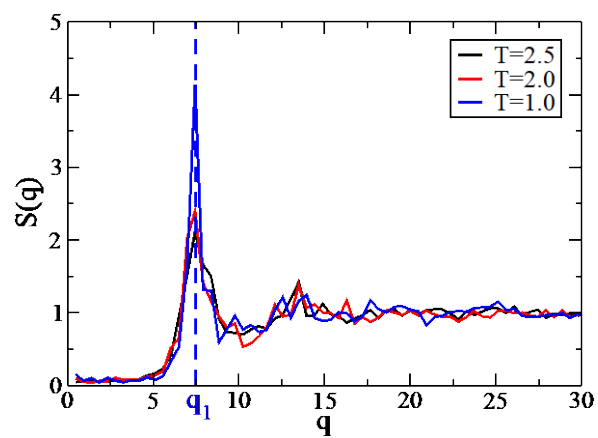


Figure S5. The structure factor $S(q)$ as function of wavevector q for $T=2.5$, 2.0 and 1.0 . The first peak position q is 7.45 .

10

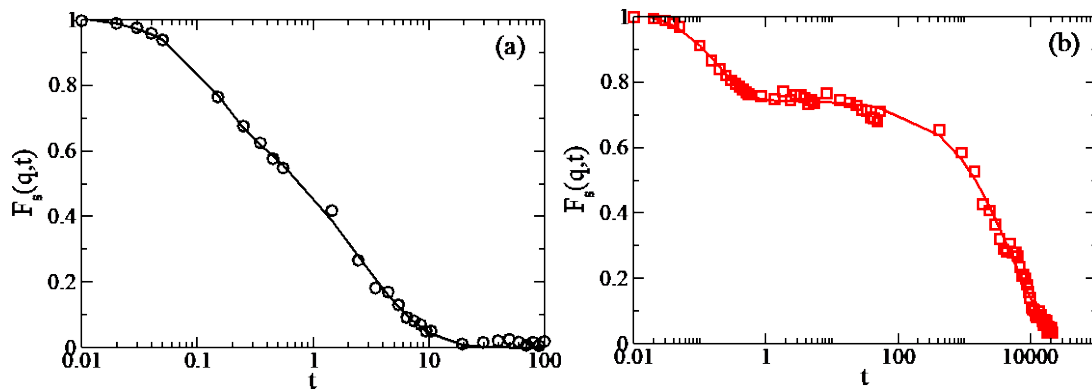
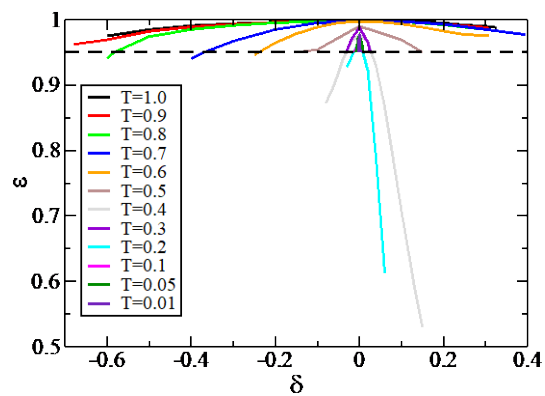


Figure S6. Self intermediate function $F_s(q,t)$ for $T=1.0$ and 0.5 . The solid curves are the ones fitted by Eq.S3.

5



5

Figure S7. The quality of the fits as a function of δ (explained in the text) for all temperatures in this work. The black dashed line is the threshold value chosen here, $\epsilon^*=0.95$.

10

15